Photodissociation dynamics of OClO: O(^3P_J) state and energy distributions

Melanie Roth, Christof Maul, and Karl-Heinz Gericke
Institut für Physikalische und Theoretische Chemie, Technische Universität Braunschweig, Hans-Sommer-Strasse 10, 38106 Braunschweig, Germany

(Received 18 August 1997; accepted 22 September 1997)

The photodissociation dynamics of OClO in the near ultraviolet (UV) was investigated in a state specific and energy selective manner. At a dissociation wavelength of 308 nm, OClO($\tilde{X}\ ^2B_1$) was excited to the OClO($\tilde{A}\ ^2A_2(18,0,0)$) state, from which it decays into ClO($X\ ^2\Pi_{3/2,1/2}$) and O($^3P_{2,1,0}$). The nascent oxygen fragments were detected spin selectively by resonant enhanced multiphoton ionization and time of flight measurements (REMPI-TOF). Based on the measurements and the conservation of energy and linear momentum, the internal energy of the ClO partner fragment was obtained. On average, more than 60% of the available energy is transferred into internal excitation of the ClO radical. Nearly the whole internal energy is vibrational energy with vibrational levels populated up to the energetic limit. Besides, the internal energy depends on the oxygen spin-orbit state because the fraction of highly excited ClO fragments increases with increasing total angular momentum J. The bimodal behavior of the fragment energy distribution indicates two different dissociation pathways, in which one leads to ClO radicals excited up to $v=10$ and the other one up to $v=15$. Furthermore, the decay is anisotropic, which was proved by polarization experiments. This is a hint for a short decay time estimated to be in the order of a few hundred femtoseconds. © *1997 American Institute of Physics.* [S0021-9606(97)02148-X]

INTRODUCTION

Photodissociative reactions play an important role in atmospheric chemistry. As Cl and ClO radicals are crucially involved in stratospheric ozone depletion, there is great interest in the photolysis of OClO. The near ultraviolet and visible photodissociation of the OClO molecule leads to two product channels, one producing O and ClO radicals and the other one generating Cl and O_2 products:

$$\mathrm{OClO}+h\nu\rightarrow \mathrm{O}(^3P_J)+\mathrm{ClO} \tag{1}$$

$$\rightarrow \mathrm{Cl}(^2P_J)+\mathrm{O_2}. \tag{2}$$

In gas phase photodissociations, the first channel is preferred with a quantum yield of about 95%. Incoherent results have been obtained on the quantum yield of the second channel.[1,2] Davis and Lee[3] published a yield of $3.9\%\pm0.8\%$ at 404 nm and less than 0.2% at wavelengths smaller than 370 nm, agreeing well with results lately obtained in our laboratory,[4] where a different detection scheme was used. Therefore, channel 2 clearly is a secondary process in the studied wavelength regime. The main channel, 1, has been investigated by determining the vibrational and rotational population of the nascent ClO fragment. The state specific detection of ClO is based on early spectroscopic work by various groups analyzing spectra obtained in the microwave,[5] infrared (IR),[6] and the vacuum ultraviolet (VUV)[7] region, characterizing the electronically excited $C\ ^2\Sigma$ state and the $X\ ^2\Pi_i$ ground state. In addition, there are laser induced fluorescence (LIF),[8,9] REMPI,[10,11] and femtosecond real-time probing[12] experiments. Based on some of those measurements, Coxon[13] calculated the molecular constants of ClO in its ground and excited state for $v=0$ and $v=1$. The spectroscopic constants of the ground level were completed by Burkholder *et al.*,[14] who observed infrared spectra of the fundamental ($v=1\leftarrow v=0$) and first overtone ($v=2\leftarrow v=0$) bands of the ClO ($X\ ^2\Pi_{3/2}$,$^2\Pi_{1/2}$) radical.

Baumgärtel and Gericke[15] showed that the two-photon LIF technique is a powerful method in detecting nascent and completely state-resolved ClO because the two-photon excitation eliminates the tedious creation of VUV photons, while the fluorescence observation in the VUV by means of a solar blind photomultiplier dramatically improves the signal to noise ratio. Davis and Lee[16] studied the dissociation dynamics of OClO at wavelengths between 350 and 475 nm. At wavelengths shorter than 400 nm they observed a release of the excess energy essentially in relative translation and not in vibration, whereas at wavelengths longer than 400 nm, nearly all thermodynamically accessible levels are populated. They supposed that most of the internal ClO energy is stored in vibration and less in rotation.

Delmdahl *et al.*[17] successfully employed the two-photon LIF excitation when investigating the state-to-state OClO photodissociation from the $\tilde{A}\ ^2A_2$ (18,0,0) and (11,0,0) levels of the symmetric stretch motion where the symmetric stretch motion is transferred into the dissociative asymmetric stretch motion on the $\tilde{A}\ ^2A_2$ surface leading to the O and ClO products. For the dissociation originating from the (18,0,0) state, Delmdahl *et al.*[17] found extremely vibrationally excited ClO. The conclusion of this work was that the energy above the dissociation barrier of the $^2A_2$ state is essentially transferred into ClO vibration. This observation is confirmed by measurements of Huber *et al.*,[18] who observed the ClO energy distribution when OClO is excited into the $\nu_1=9$ to $\nu_1=18$ levels. They used photofragment translational energy spectroscopy and detected the ClO fragment with a conventional quadrupole mass spectrometer.

Though the OClO photodissociation has been investi-

gated with the REMPI technique[19,20] and the O atom is easily accessed by REMPI,[21,22] the experimenters concentrated on measuring ClO and Cl fragments, but no oxygen fragment analysis has been performed. In this work, for the first time REMPI spectra of the oxygen fragments are presented, formed by dissociation of OClO ($\tilde{A}\ ^2A_2(18,0,0)$) upon excitation at 308 nm. We state selectively probed all spin-orbit states of oxygen O(^3P_J) with (2+1)-REMPI at wavelengths around 225 nm. Analyzing state specific velocity distributions by time of flight measurements, kinetic and internal energies of the ClO partner fragment are obtained, taking into account the conservation of energy and linear momentum. Thus, the energetics and the (joint partner) product state distributions of the photodissociation process can completely be characterized, especially with respect to the dissociation pathways leading to spectroscopically dark, highly vibrationally excited ClO fragments. Furthermore, new dissociation pathways were found with a rise in excitation energy but their dissociation geometry, decay time, and spatial distribution is still unknown. In addition, we present high resolution REMPI spectra of the spectroscopically accessible ClO which were investigated by Vaida *et al.*[23] at lower resolution. In order to obtain some information on the dissociation time, polarization measurements were performed, and the influence of the polarization vector of the probe laser on the shape of the TOF profile, reflecting the spatial fragment distribution, was analyzed.

The generation of highly vibrationally excited ClO in the photodissociation of OClO is of great importance in atmospheric chemistry because of possible subsequent ClO reactions with constituents of the atmosphere.

Choo and Leu[24] suggested the following reactions of vibrationally excited ClO with Cl and O_3:

$$\mathrm{ClO}(v>2)+\mathrm{Cl}\rightarrow \mathrm{Cl_2}+\mathrm{O}, \tag{3}$$

$$\mathrm{ClO}(v\gg 0)+\mathrm{O_3}\rightarrow \mathrm{ClO}+\mathrm{O_2}+\mathrm{O}. \tag{4}$$

Similarly, the UV dissociation of O_3 at 226 nm ($O_3+h\nu(226\ \mathrm{nm})\rightarrow O_2+O$) is known[25] to produce highly vibrationally excited $O_2(X\ ^3\Sigma_g^-, v\geqslant 26)$ molecules, which could be a so far neglected source in the atmospheric ozone production via the reaction,

$$\mathrm{O_2}(v\geqslant 26)+\mathrm{O_2}\rightarrow \mathrm{O_3}+\mathrm{O}(^3P). \tag{5}$$

Furthermore, a vibrationally excited oxygen molecule can be dissociated by near UV radiation, whereas O_2 in its ground level requires VUV[26] radiation. As a result of the higher flux of near UV light in the atmosphere, this oxygen dissociation pathway becomes important for atmospheric chemistry.

Due to the formation of extremely vibrationally excited ClO radicals, reactions with the atmospheric molecules O_2 or N_2 become possible, and in this case the reaction rate may well exceed the relaxation rate.

EXPERIMENT

The OClO molecule was generated according to the method of Derby and Hutchinson.[27] A bulb containing a gas mixture of about 10% Cl_2 and 90% N_2 was coupled to a column filled with $NaClO_2$ and Raschig rings. While the gas flowed through the column, OClO and NaCl were produced. The gas was transferred into the reaction chamber without further purification. The cell was evacuated by two oil diffusion pumps (Leybold, 500 l/s) and a turbomolecular pump (Leybold Heraeus 360 CSV, 360 l/s) to a base pressure of 10^{-4} Pa. The OClO gas was expanded into the reaction chamber by a pulsed nozzle (General Valve) which was operated at a stagnation pressure of 200–600 mbar and a pulse duration of typically 250 μs. At a repetition rate of 10 Hz, the background pressure was 10^{-3}Pa with the nozzle in operation. From linewidth measurements with CO, the parent molecule temperature could be estimated to be about 10 K. Thus, the internal energy of OClO is negligible.

The molecular beam propagates perpendicularly to the axis of our time of flight spectrometer, which is described in detail elsewhere.[28] At the end of the spectrometer, microchannel plates in chevron configuration are used to enhance the ion signal. The TOF spectrometer can be operated in three different ways.

First, in the drift mode the ions drift through the spectrometer with a total length $s=0.57$m only because of their initial recoil velocity. The signal is monitored with a multihit time-to-digital converter (FAST 7885) with a time resolution of 5 ns per channel, stored in a data buffer (FAST MCD/PC) and transferred to a personal computer. The drift mode directly yields the velocity distribution $F_v(v)$ from the measured TOF profile $F_T^D(t)$ via the relation

$$F_v(v)=F_T^D(t)\cdot t^2. \tag{6}$$

Second, in the acceleration mode, the ions are accelerated along a region of 0.19 m ($=s/3$) by a homogeneous electric field of variable strength. In the present measurements the electric field was fixed at 2600 V/m. The acceleration region is followed by a field free drift region of twice the length of the acceleration region. The shape of the temporally broadened ion signal was monitored by a digital transient wave form recorder (LeCroy 9450). The acceleration mode yields the distribution $F_{v_x}(v_x)$ of the velocity component v_x along the spectrometer axis from the TOF profile $F_T^A(\Delta t)$ via the linear relationship

$$v_x=c'\cdot\Delta t, \tag{7}$$

where $c'=8s/3t_0^2=8eU_A/m$ accounts for the acceleration voltage U_A, the spectrometer length s, particle mass m, and charge e. $\Delta t=t-t_0$ is the deviation from the center of the acceleration profile.

Equation (7) holds in all practically relevant cases, where the acceleration energy is large compared to the initial kinetic energy of the observed fragment:

$$e\cdot U_A\gg E_{\mathrm{kin}}=\tfrac{1}{2}mv^2. \tag{8}$$

$F_v(v)$ is easily obtained from $F_{v_x}(v_x)$ if the spatial fragment distribution is known.

Third, in the Doppler mode the electric field is so large that one cannot measure any difference in arrival time. Instead the total intensity of the ion signal is integrated by a

boxcar integrator and averager (Stanford Research System SR 250) and digitized by an A/D converter while the laser is tuned over the Doppler line. In the Doppler mode the distribution $F_{v_y}(v_y)$ is obtained, similarly as in the preceding paragraph, from the Doppler broadened line shape $D(\Delta\nu)$ via the relation,

$$v_y = \frac{c\Delta\nu}{\nu_0}, \tag{9}$$

where c is the speed of light, v_y is the velocity component along the laser beam, ν_0 is the center of the Doppler line, and $\Delta\nu = \nu - \nu_0$ is the frequency deviation from the line center. If the dissociation process is isotropic, $F_{v_x}(v_x)$ and $F_{v_y}(v_y)$ are equal.

The high temporal resolution of TOF profiles obtained in the drift mode allows a very accurate determination of the underlying velocity distribution. The acceleration profiles compensate for the decreasing spectrometer transit efficiency for low kinetic energies, although at the expense of temporal resolution. Thus, operating the spectrometer in both modes combines the respective advantages and yields highly accurate, complete velocity distributions.[29]

An excimer pumped dye laser system (Lambda Physik LPX 605*i* [XeCl 308 nm], LPD 3000) delivered the photolysis and probe pulses. A small part of the pump light was coupled out by a beam splitter and was used to photolyze the molecule. An optical delay line formed the jitter-free timing between photolysis and probe pulse. The laser pulses were electronically delayed with respect to the molecular beam (Stanford Research System DG 535).

The oxygen fragments $O(^3P_{2,1,0})$ in their different spin-orbit states were probed by (2+1)-REMPI in the wavelength region of 225 nm. In order to obtain this wavelength we used Coumarin 47 (440–484 nm, 5–10 mJ/pulse) and a β-barium borate (BBO) crystal for second harmonic generation (50–200 μJ/pulse). The light pulses counterpropagated in the reaction chamber and both intersected the spectrometer axis perpendicularly. The molecular beam intersected the probe pulse in an angle of 54°. In order to determine anisotropic effects in the photodissociation of OClO we polarized the photolysis laser parallel and perpendicular to the spectrometer axis $\vec{s}$. The polarization of the analyzing dye laser light was always maintained parallel to the spectrometer axis.

The photolysis and probe pulse were focused in the reaction chamber. The photolysis light was focused by a 150 mm lens in the Doppler and the acceleration mode, whereas for the drift mode a 100 mm lens was used. The probe pulse was focused by a 80 mm lens for the acceleration and drift profiles, for the Doppler profiles by a 135 mm lens.

The other partner fragment ClO was detected in the Doppler mode only by a one-color experiment with RDC 360 (342–373 nm, 7–10 mJ/pulse) as laser dye. In that case OClO photolysis and ClO detection occur at the same wavelength. Since the flight times of ^{35}ClO and ^{37}ClO differ by their masses, isotope specific spectra were observed simultaneously by adjusting two boxcar gates at the respective arrival times. The signals were normalized by measuring the probe laser intensity.

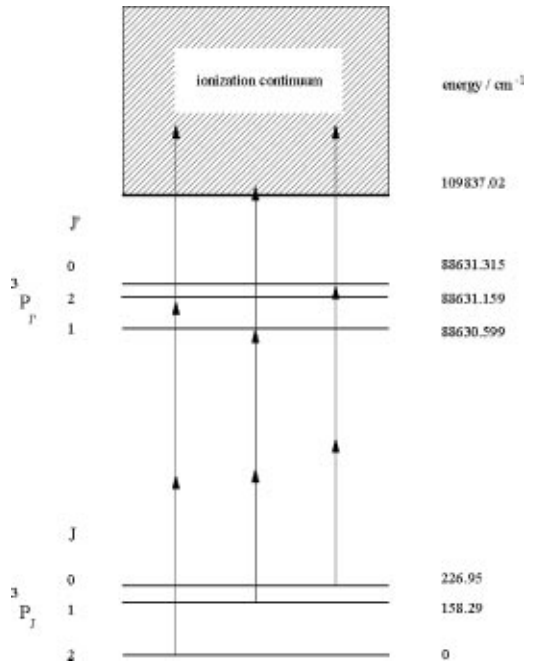

FIG. 1. Term scheme of the oxygen atom which contains the (2+1)-REMPI transitions of every spin-orbit state. The energy levels are not scaled.

RESULTS

In the photodissociation of OClO the oxygen fragment is formed in its ^3P_J ground state, where its angular momentum quantum number has the values $J=0,1,2$. The energy levels of these states are separated by 158 and 227 cm^{-1} as it is indicated by the term scheme in Fig. 1. Using transitions $3p\ ^3P_J \leftarrow 2p\ ^3P_J$ with $\Delta J=0$, we detected the different spin-orbit states by (2+1)-REMPI. The $O(^3P_2)$ state was probed at 225.572, $O(^3P_1)$ at 225.974, and $O(^3P_0)$ at 226.149 nm.

Conservation of linear momentum and energy allows a calculation of maximum oxygen recoil velocity. The available energy E_{av} is the difference between photolysis energy $h\nu$ and dissociation energy E_D (19 311 cm^{-1}),[30] added to the internal energy of the parent molecule, $E_{int}(OClO)$: $E_{av} = h\nu$ (308 nm) $- E_D + E_{int}(OClO)$. In the molecular beam the parent molecule is jet cooled, and thus its internal energy $E_{int}(OClO)$ is negligible and a value of $E_{av}=13\,157$ cm^{-1} is calculated. The available energy is distributed into the kinetic energy E_{kin} and internal energy E_{int} of the fragments. The kinetic energy of the ClO fragment is that of the oxygen fragment weighted by the fragment mass ratio, which is a consequence of the conservation of linear momentum. The internal energy $E_{int}(O)$ of the oxygen atom is given by the spin-orbit state energies (see Fig. 1),

$$E_{av} = E_{int}(O) + \left(1 + \frac{m_O}{m_{ClO}}\right) E_{kin}(O) + E_{int}(ClO). \tag{10}$$

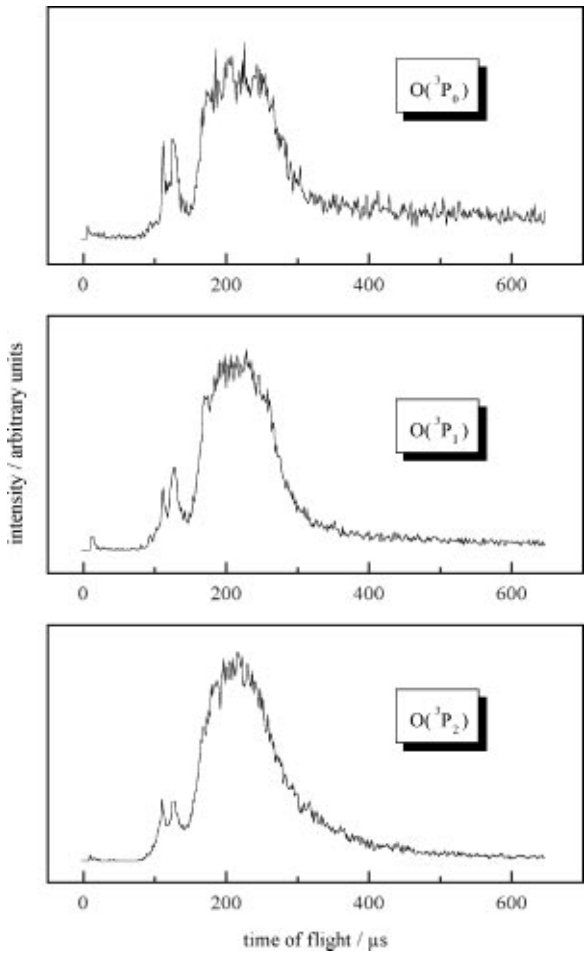

FIG. 2. Drift profiles of oxygen in different spin-orbit states ($O\,^3P_J, J=0,1,2$) containing three peaks. The first peak corresponds to photolysis of OClO at 225 nm, the second one to secondary photolysis of ClO at 308 nm and the main peak to photolysis at 308 nm.

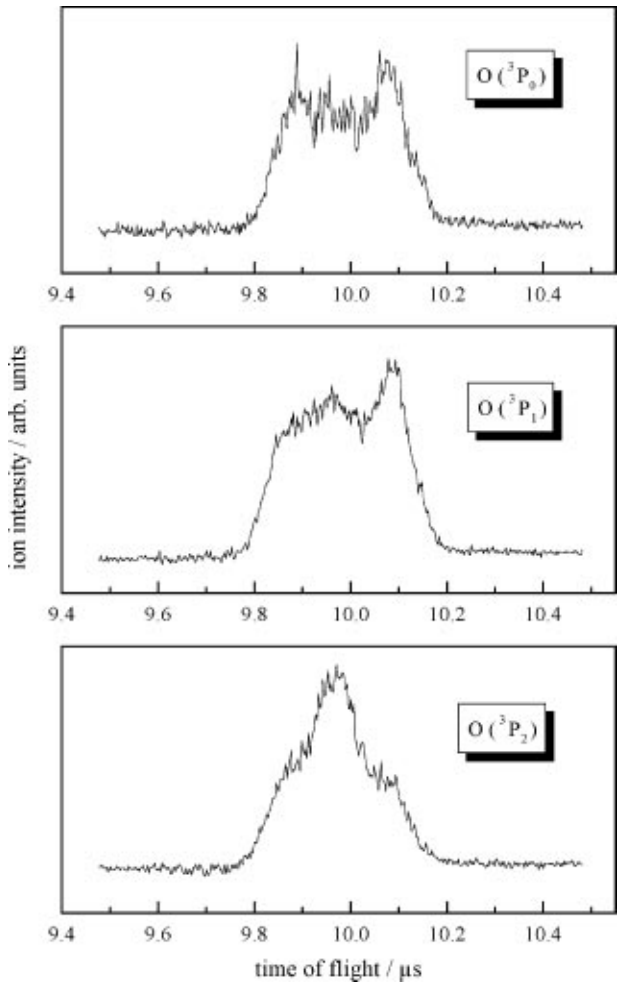

FIG. 3. TOF profiles obtained by acceleration of the generated oxygen fragments with an electric field ($U_b=500$ V, unpolarized photolysis). For $O(^3P_2)$ the highest contribution of slow O fragments is observed.

The oxygen velocity is at its maximum when the ClO radical has no internal energy. Thus, the maximum velocities of $O(^3P_2)$, $O(^3P_1)$, and $O(^3P_0)$ are 3870, 3847 and 3836 m/s, respectively.

In Fig. 2 the drift profiles of the oxygen in its spin-orbit states $(O(^3P_J), J=0,1,2)$ are shown. Of the three peaks, the main peak is caused by photolysis of OClO at 308 nm. If the ascending slope of this peak at short flight times is extrapolated to the time axis, the maximum O recoil velocity can be determined. The obtained value of 3900 ± 100 m/s is in good agreement with the calculated values according to Eq. (10).

The first peak in Fig. 2, corresponding to a value of 5200 m/s, is oxygen formed in the photolysis of OClO by a photon of 225 nm (probe pulse), and the second peak represents the fast oxygen radicals generated in the secondary photolysis at 308 nm, where a second photon dissociates the ClO fragment into Cl and O. In this case the total oxygen velocity is given by the sum and difference of the ClO parent molecule velocity as a consequence of the primary photolysis and the oxygen velocity of the secondary photolysis. The slow oxygen radicals obtained via secondary photolysis cannot be distinguished from the oxygen fragments formed in primary photolysis because of their low intensity.

At a first glance there is no remarkable difference between the profiles, so that the velocity distribution seems to be independent of the spin-orbit state. However, these drift profiles are not sensitive to slow recoil velocities and reliable conclusions can only be drawn when the acceleration profiles are taken into account. The results of these measurements are shown in Fig. 3. These profiles were measured using unpolarized probe light, so that possible anisotropic effects of the fragmentation process on the profiles are strongly reduced. In contrast to the profiles of $O(^3P_1)$ and $O(^3P_0)$, the $O(^3P_2)$ profile shows an increase of intensity in the middle of the peak, which indicates the preferred formation of slow atoms generated in the $J=2$ state.

In order to test any anisotropic behavior of the dissociation process we polarized the photolysis laser parallel and perpendicular to the spectrometer axis $\vec{s}$. For an isotropic dissociation pattern the profiles should have the same appearance. However, the obtained profiles presented in Fig. 4 and Fig. 5 differ significantly, which is an indication of an anisotropic fragmentation. Moreover, this proves that the dis-

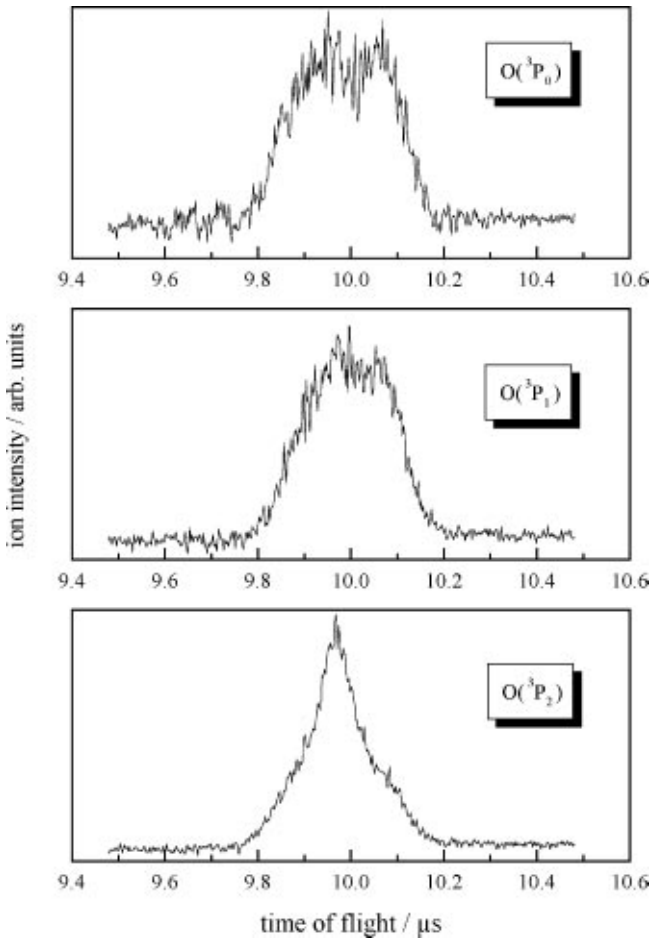

FIG. 4. Acceleration profiles measured with the photolysis light being polarized perpendicular to the spectrometer axis, where the oxygen fragments are preferentially generated perpendicular to the spectrometer axis.

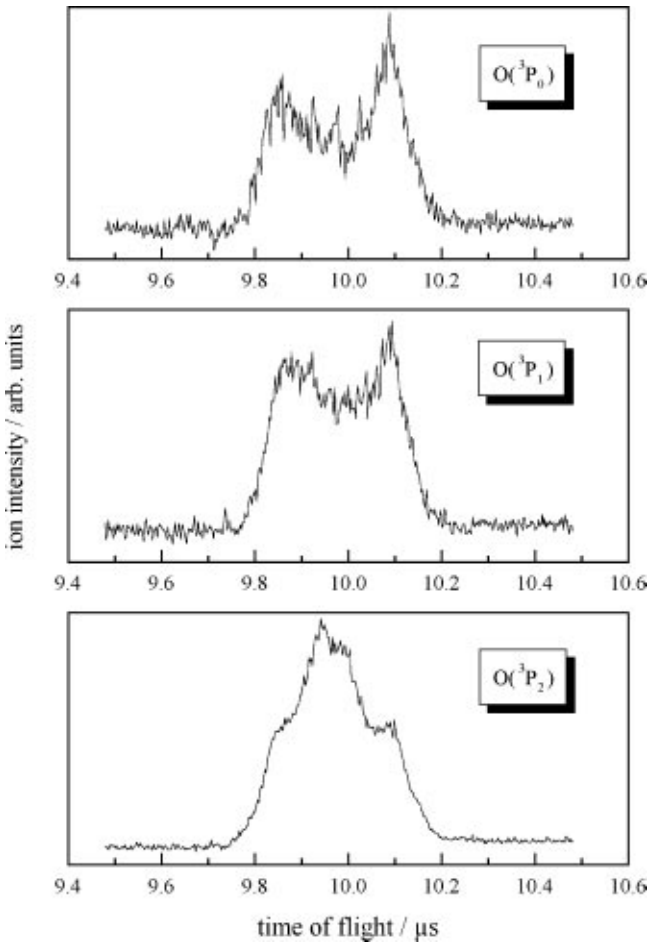

FIG. 5. Acceleration profiles measured with the photolysis light polarized parallel to the spectrometer axis, where the oxygen fragments are preferentially generated in or against the direction of the detector.

sociation has to be fast because otherwise the anisotropic effects would be strongly reduced due to parent molecular rotation. The transition dipole moment of OClO ($\tilde{A}\ ^2A_2 \leftarrow \tilde{X}\ ^2B_1$) lies in the molecular plane, parallel to the line connecting the two oxygen atoms. Under the assumption that the dissociation is very fast, the valence angle of the ground state is maintained in the excitation. If the O fragment recoils from the center of mass of the ClO partner, the velocity vector forms an angle of 17.6° with respect to the dipole moment (see Fig. 6). Consequently, the O fragments are mainly generated perpendicular to the spectrometer axis $\vec{s}$ if the photolysis light is polarized perpendicular to $\vec{s}$, and the signal intensity at the line center will be increased (Fig. 4). On the other hand, if the photolysis pulse is polarized parallel to $\vec{s}$, the O atoms are mainly formed in or against the direction of $\vec{s}$ (Fig. 5). Consequently, there is a dip in the center of the acceleration profile.

The angle dependent velocity distribution $F_v(\theta,v)$ can be described by $F_v(v)$ and a term containing the anisotropy parameter β:

$$F_v(\theta,v) \propto \frac{F_v(v)}{v}\,[1+\beta P_2(\cos\,\theta)], \tag{11}$$

if no correlation between β and $F_v(v)$ exists.[31] $P_2(\cos\,\theta)$ is the second Legendre polynomial of the polar angle θ with respect to the transition dipole moment μ. The second term in brackets has to vanish to obtain a distribution independent

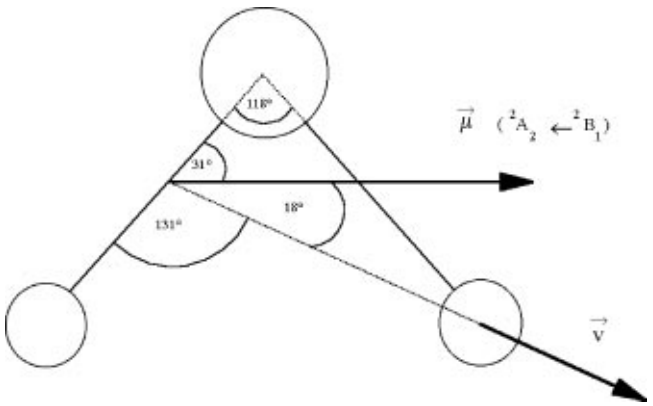

FIG. 6. Recoil angle of the O fragment calculated under the assumption that the angle of the ground level remains constant during fragmentation and the O fragment recoils from the center of mass of the ClO fragment.

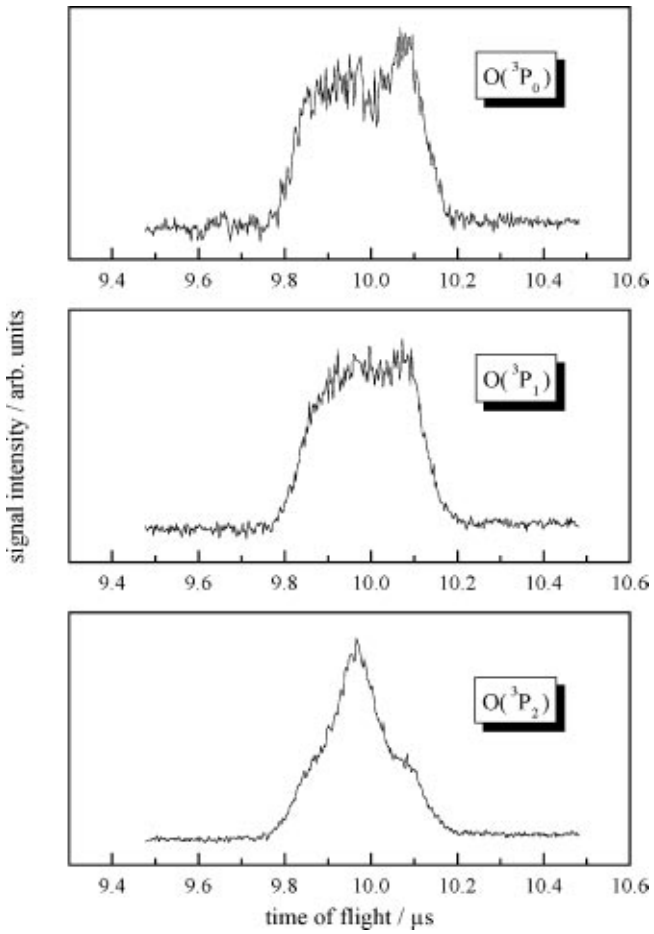

FIG. 7. Calculated acceleration profiles based on the profiles obtained by polarizing the photolysis light parallel and perpendicular to the spectrometer axis.

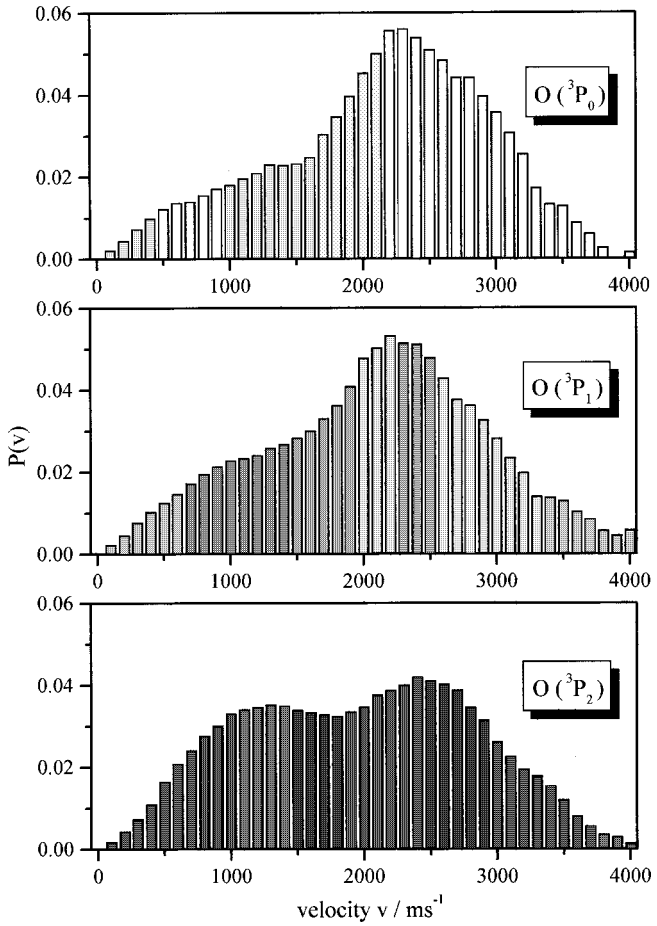

FIG. 8. O(^3P_J) velocity distributions received by the combination of acceleration and drift profiles.

of the spatial distribution of the fragments. Since the anisotropy parameter exhibits a value different from zero, the Legendre polynomial has to fulfill the condition

$$P_2(\cos\ \theta_m)=\tfrac{1}{2}(3\cos^2\ \theta_m-1)=0, \tag{12}$$

where $\theta_m=54.7°$ is the so-called magic angle. In order to obtain the acceleration profiles of the magic angle, profiles of both polarizations were normalized separately to equal areas and summed up with suitable factors according to a procedure first described by Huber and co-workers.[32] The result is shown in Fig. 7.

Based on the acceleration and drift profiles, the velocity distribution of every state is calculated and the results are presented in Fig. 8. All obtained distributions show bimodal behavior, but the velocity distribution of the O($^3P_2$) contains more slow ions than that of the O($^3P_0$) or O($^3P_1$).

The obtained velocity distributions can be used to calculate Doppler profiles. These calculated Doppler profiles are in good agreement with the measured ones, indicating the conformance between the drift, acceleration, and Doppler profiles. Integration of Doppler profiles obtained under equal conditions yields a population relation of O($^3P_2$):O($^3P_1$):O($^3P_0$)=0.53: 0.32: 0.15, which is comparable to a statistical distribution (0.56: 0.33: 0.11).

In order to test whether the high vibrational excitation of the ClO radical is directly measurable in detecting ClO itself, we observed REMPI one-color spectra of ClO in the wavelength region of 338–356 nm, which are presented in Fig. 9. The spectra are normalized to the laser intensity and are isotope specific because of the difference in mass of ^{35}ClO and

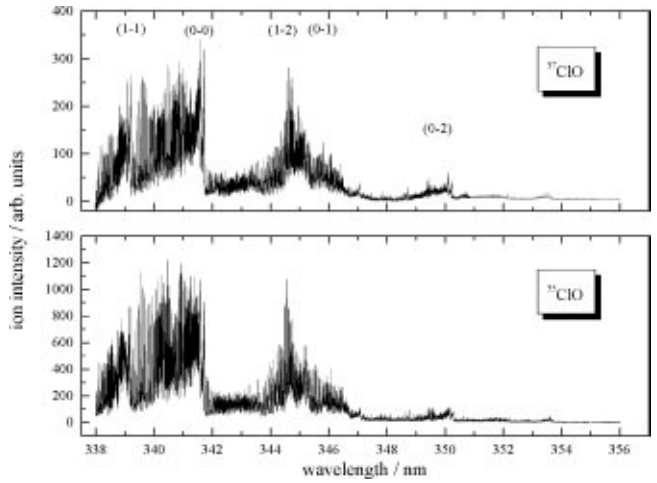

FIG. 9. One-color spectra of ^{35}ClO and ^{37}ClO with the natural isotope relation ^{35}Cl:^{37}Cl=3:1 reflected in the intensity of the lines.

^{37}ClO. The signal intensity of both isotopes reflects the natural isotope relation of ^{35}Cl:^{37}Cl=3:1. The vibrational bands are assigned in Fig. 9. The $^2\Pi_{3/2}$ spin system is energetically higher than the $^2\Pi_{1/2}$ spin system and is less populated. The observed ClO is vibrationally excited up to $v=3$, while the intensity of the vibrational bands decreases with increasing v. Comparatively few rotational lines are observed, so the rotational excitation is low. This behavior is comparable to the results of Vaida *et al.* at 339–342 nm, but the rotational lines are monitored with much better resolution.[23] Unfortunately, unfavorable Franck–Condon factors do not allow direct monitoring of the ClO fragments for $v>5$, as is shown in earlier LIF measurements.[15] Therefore, the analysis for the highly vibrationally excited states of ClO has to rely on the O atom observations.

DISCUSSION

The observed velocity distributions of the O($^3P_2$), O($^3P_1$), and O($^3P_0$) products are bimodal in character, which is also reflected in the energy distributions. The slow oxygen fragment corresponds to a ClO fragment with extremely high internal energy. The contribution of slow ions increases with increasing J from 20% for O($^3P_0$) to 32% for O($^3P_2$), so that together with the O($^3P_2$) state the highest portion of highly excited ClO radicals is found. Using Eq. (10) and the kinetic energy of the O fragments, the internal energy of the ClO fragment is calculated. The computed internal energy distributions are presented in Fig. 10. We found ClO fragments with extremely high internal energy of about 8000 and 12 500 cm^{-1}, respectively, in agreement with Delmdahl *et al.*.[17] The decay of a molecule is influenced by the potential surfaces of its electronic levels. Figure 11 shows cuts through *ab initio* potential surfaces calculated by Peterson and Werner with respect to symmetric and asymmetric bond length distortion and variation of the valence angle.[33] If the bond lengths are varied asymmetrically, the molecule takes on C_s symmetry, otherwise C_{2v} symmetry. Both symmetries are described with different notations. In Fig. 11 the C_s notation is used, whereas in the text we will use C_{2v} notation. The alternative notation is added in brackets to facilitate the comparison. The $\tilde{A}\ ^2A_2$ and $^2B_2$ surfaces are bonding with respect to both the symmetric OClO distance r_{ClO} and the valence angle φ because of their potential minimum. If the molecule fragments via the $\tilde{A}\ ^2A_2[^2A'']$ and $^2A_1[^2A']$ surfaces with respect to asymmetric bond length distortion R_{ClO}, it has to overcome an energy barrier. The potential surface of the $\tilde{A}\ ^2A_2$ state exhibits a barrier E_b with respect to the R_{ClO} coordinate. If the excitation energy is sufficiently high, the dissociation could follow a dissociation channel, where a vibrational predissociation along the v_3 coordinate takes place. Although the molecule is initially bound in the $\tilde{A}\ ^2A_2$ level along the symmetric stretching mode v_1, a small coupling between v_1 and v_3 is enough to change into the asymmetric system while the energy is transformed into asymmetric core movement. As soon as enough energy is transferred into the asymmetric bond length distortion to overcome the barrier, the OClO can fragment into a vibrationally excited ClO and an O radical.

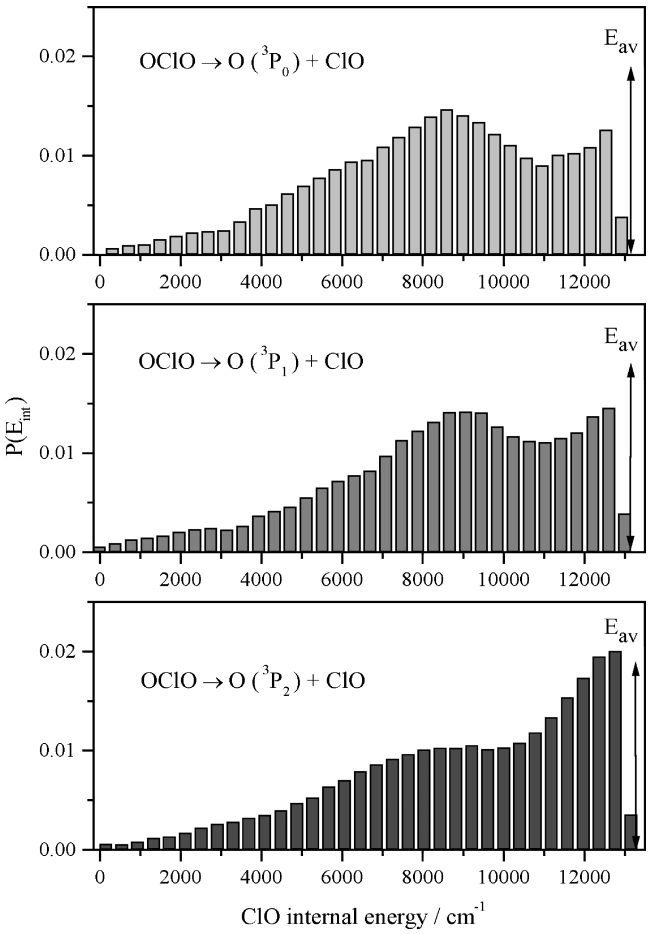

FIG. 10. Internal energy distribution of ClO for different O(^3P_J) partner fragments. Remarkable is the bimodal behavior and the increasing fraction of highly internally excited ClO products with increasing J of the partner atom.

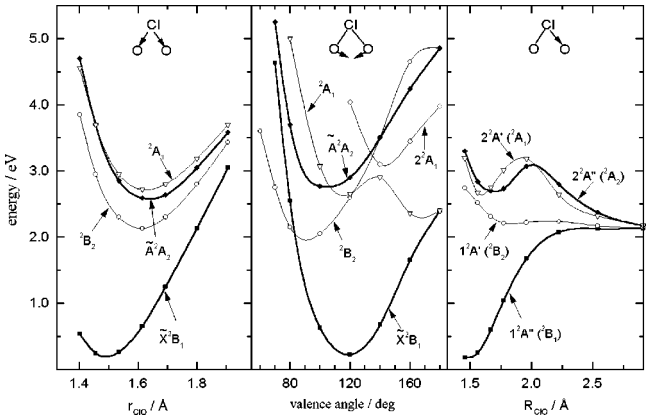

FIG. 11. Cuts through *ab initio* potential energy surfaces calculated by Peterson and Werner (Ref. 33) for variation of the symmetric stretch coordinate R_{ClO}, the bending coordinate φ, and the asymmetric stretch coordinate r_{ClO}.

TABLE I. State selective energy partitioning for the different $O(^3P_J)$ states.

Spin-orbit state	Fraction of the total oxygen signal	$E_{int}(O)/E_{av}$ $E_{int}(O)[cm^{-1}]$	$E_{int}(ClO)/E_{av}$ $E_{int}(ClO)[cm^{-1}]$	$E_{kin}(O)/E_{av}$ $E_{kin}(O)[cm^{-1}]$	$E_{kin}(ClO)/E_{av}$ $E_{kin}(ClO)[cm^{-1}]$
$O(^3P_2)$	0.53	0%	70%	23%	7%
		0 cm^{-1}	9122 cm^{-1}	3071 cm^{-1}	964 cm^{-1}
$O(^3P_1)$	0.32	1%	66%	25%	8%
		158 cm^{-1}	8696 cm^{-1}	3275 cm^{-1}	1028 cm^{-1}
$O(^3P_0)$	0.15	2%	63%	27%	8%
		227 cm^{-1}	8337 cm^{-1}	3496 cm^{-1}	1097 cm^{-1}
average		0.6%	67.7%	24.2%	7.5%

The minimum of the $^2A_1$ surface with respect to the valence angle is obtained for a value of 180° whereas the minimum of the $\tilde{A}\ ^2A_2$ level corresponds to an angle of 107°. A change of the valence angle induces a torque which should be reflected in high rotational energy. Since only low rotational energy was observed in the experiment, a decay on the $^2A_1$ surface is improbable. An intramolecular transition from the $\tilde{A}\ ^2A_2$ surface to the ground level $\tilde{X}\ ^2B_1$ and a subsequent decay should lead to a statistically distributed ClO fragment energy which is also in contrast to the experiments,[17] and therefore the mechanism is equally unlikely.

Characteristic for our measurements are the extremely high internal energy of ClO and the anisotropic distribution of the products. The anisotropic behavior indicates a fast decay, i.e., the lifetime of excited OClO is less than a rotational period of the molecule. Otherwise the originally aligned molecules would lose their alignment by rotation. The average time of rotation T_r is given by

$$T_r = 2\pi \sqrt{\sum_i (\theta_i/3)RT}, \tag{13}$$

where θ_i are the moments of inertia, R is the gas constant, and T is the temperature.[34] With a temperature of 10 K, a rotational period of about 15 ps is calculated, which is an upper limit. Using the linewidths of the absorption spectrum at 296 K measured by Wahner *et al.*, the lower limit of the lifetime of the OClO(18,0,0) state could be estimated to about 0.2 ps.[35]

The bimodal behavior of the internal energy distribution refers to different dissociation channels. Because of the fast decay it is probable that the OClO molecule directly dissociates on the excited $\tilde{A}\ ^2A_2$ potential surface if the excitation energy overcomes the barrier. This should be reflected in highly vibrationally excited ClO radicals, which comes from the initial vibrational excitation of OClO. In that case the excited OClO molecule nearly decays under a perpendicular geometry. The equilibrium angle of the $\tilde{A}\ ^2A_2$ state is about 118°. Therefore, the oxygen radical could hardly transfer vibrational energy into ClO while it is repelled.

One can estimate the rotational energy of the ClO fragment by different model calculations. If the parent molecule OClO does not rotate, the mean rotational energy can be calculated from the zero point motion of the υ_2 vibration:

$$\langle E_{rot}\rangle_{ClO} = \tfrac{1}{8}\omega_2 \frac{m_{Cl} + m_O(1-\cos\ \varphi_0)}{m_{ClO}}, \tag{14}$$

where ω_2 is the energy of the bending vibrational mode υ_2, and $\varphi_0 = 117.7°$ is the bending angle of the OClO ground level.[36] Based on Eq. (14) we calculate a value of 65 cm^{-1}.

In the impulsive model, a triatomic molecule ABC decays because of an instantaneous development of a repulsive force between the departing atom A, and the atom B it was initially bound to. This force is directed along the breaking bond. Therefore, a torque on the diatom BC around its center of mass is induced. Consequently BC is rotationally excited and the rotational angular momentum is directed perpendicular to the molecular plane. The third atom C is not involved in the dissociation process. According to the impulsive model, the limitations of which are shown by Schinke,[37] the rotational energy can be calculated by:

$$E_{rot} = E_{av} \frac{\sin^2\ \varphi_0 m_O^2}{(m_O + m_{Cl})^2 - m_O^2 \cos^2\ \varphi_0}. \tag{15}$$

We obtain a rotational energy of 1037 cm^{-1}. Both calculations indicate that the rotational energy is small compared to the total internal ClO energy of about 8900 cm^{-1}, agreeing with the results of Huber *et al.*, which are based on a rotational energy of 650 cm^{-1}.[18]

The energy difference $(h\nu\text{-}E_b)$ between excitation energy $h\nu$ and barrier E_b is mainly transformed into internal energy of the ClO fragment. The remaining kinetic energy of the fragments is equal to $(E_b - E_D)$. We observed a mean internal ClO energy of 8900 cm^{-1}, which corresponds to a vibrational excitation around $\upsilon = 10$. That way an energy barrier of 23 500 cm^{-1} results from dissociation energy and kinetic energy. The conclusion that the surplus energy $(h\nu - E_b)$ is released as ClO vibration is supported by recent experimental results. Huber *et al.* observed an increase of internal ClO energy with increasing available energy, whereas the average translational energy E_{kin} (ClO+O) remains constant, ranging from 4200 to 4600 cm^{-1}.[18] Delmdahl *et al.* examined the OClO dissociation of the $(\tilde{A}\ ^2A_2(11,0,0))$ state where the OClO molecule was excited at 351 nm.[17] From the energy balance they expected ClO radicals vibrationally excited to $\upsilon = 3$, which was manifested by their measurements. In our experiment we observed the percentages of the available energy which were transferred in

TABLE II. ClO fragments with sufficient energy to react with N_2.

Spin-orbit state	Fraction of the total oxygen signal	Percentage of ClO radicals following the second dissociation pathway	Percentage of ClO radicals with an internal energy higher than 8500 cm^{-1}
$O(^3P_2)$	0.53	32%	62%
$O(^3P_1)$	0.32	24%	54%
$O(^3P_0)$	0.15	20%	49%
average		27.6%	57.5%

internal and kinetic energy shown in Table I. The main part of about 68% is found in internal ClO excitation. The kinetic energy is nearly constant and its value is in good agreement with that of Huber *et al.*.[18]

While the first maximum (at low internal energy) of the ClO internal energy can be explained by this decay mechanism on the $\tilde{A}\ ^2A_2$ surface, it seems very unlikely that the second maximum (at high internal energy) can be explained by a decay on the same surface.

The second dissociation mechanism might presumably occur on the $^2B_2[^2A']$ surface. At an excitation energy of 32 468 cm^{-1}, the potential surfaces of the $\tilde{A}\ ^2A_2$ and $^2A_1$ levels are close together and the crossing is smooth (see Fig. 11). Thus, a fast $\tilde{A}\ ^2A_2 \leftarrow ^2A_1$ transition can be expected. A possibly following vibronic, and, therefore, likewise fast coupling with the $^2B_2[^2A']$ surface leads to the dissociation. On this surface the molecule decays at a bending angle of about 180° that presumably causes high vibrational energy. If it is assumed that the energy difference between the excitation energy and the minimum of the $^2B_2[^2A']$ surface determines the internal energy of the ClO fragment, the internal energy could receive nearly the whole available energy (E_{av}=13 157 cm^{-1}). Thus, the observed second peak in the energy distribution at about 12 500 cm^{-1} is favorably explained by this decay mechanism.

The amount of ClO fragments being generated via the second dissociation pathway depends on the spin-orbit state of the O partner atom and increases with increasing J. We calculated the contribution of each spin-orbit state by integrating the internal energy from 11 000 cm^{-1} to E_{av} and normalizing it to the total internal ClO energy. The results are shown in Table II. In the $O(^3P_2)$ state, 32%, in the other states, 24% and 20% respectively, of the ClO fragments follow the second dissociation pathway.

The high vibrational excitation of the ClO radical allows reactions which are normally thermally prevented by the activation energy, and endothermic reactions become possible. A reaction with chlorine and ozone [see Eqs. (3) and (4)] is unlikely because relaxation measurements of ClO ($v \leqslant 6$) with N_2 indicate that the vibrational relaxation rate is too high to allow a significant amount of ClO (v) reactions. However, the reaction with N_2 is energetically allowed for $v > 9$, according to

$$ClO(v \geqslant 0) + N_2 \rightarrow N_2O + Cl, \quad \Delta H_r = 8500\ cm^{-1}, \quad (16)$$

with the Cl product itself catalyzing the ozone decomposition.[38,39] The calculation of the standard reaction enthalpy is based on recommended values of the standard enthalpy of formation for reactants in their respective ground states.[40] We computed the portion of ClO radicals having enough energy to follow the reaction with N_2; the results are also summarized in Table II. On average more than 50% of the ClO fragments have sufficient energy to react with N_2.

In order to determine the impact of extremely vibrationally excited ClO on the atmosphere, the dissociation dynamics of other OClO vibrational states with respect to their spin selective behavior should also be investigated. This is, in principle, possible because it only requires another tunable laser system so that the excitation energy is variable.

CONCLUSION

The OClO dissociation was investigated by REMPI-TOF measurements of the $O(^3P_J)$ and $ClO(^2\Pi_\Omega)$ fragments. The dissociation leads to highly vibrationally excited ClO and correspondingly slow $O(^3P_J)$ fragments. The bimodal behavior of the velocity and energy distributions leads us to conclude that the fragmentation follows two different dissociation pathways with a broad velocity distribution. Channeling the vibrational energy of the excited OClO into the asymmetric stretch coordinate, the parent molecule decays via a barrier on the $\tilde{A}\ ^2A_2$ potential energy surface, releasing the difference between photon energy and barrier height as ClO vibration. Extremely vibrationally excited ClO is likely to be produced following conversion of the OClO from the initially excited $^2A_2$ surface to the $^2B_2$ surface, releasing the total available energy into ClO internal energy. The fragmentation process is spin selective. The fraction of highly vibrationally excited ClO increases with increasing J of the oxygen partner fragment. As an anisotropic spatial distribution is observable, the decay time is expected to be of the order of a few hundred femtoseconds.

The extreme internal excitation of the ClO product opens up new reaction schemes in atmospheric chemistry, such as the reaction of ClO with N_2. Therefore the OClO dissociation needs to be considered as a possible chlorine atom source in the atmosphere.

ACKNOWLEDGMENTS

We acknowledge financial support of the Deutsche Forschungsgemeinschaft. M.R. thanks the Fonds der Chemischen Industrie for fellowship support.

[1] W. G. Lawrence, K. C. Clemitshaw, and V. A. Apakarian, J. Geophys. Res. **95**, 591 (1991).
[2] E. Bishenden, P. D. Hammer, and C. J. Howard, J. Chem. Phys. **95**, 2113 (1991).
[3] H. F. Davis and Y. T. Lee, J. Phys. Chem. **96**, 5681 (1992).
[4] R. F. Delmdahl (unpublished).
[5] R. K. Kakar, E. A. Cohen, and M. Geller, J. Mol. Spectrosc. **70**, 243 (1978).
[6] R. T. Menzies, J. S. Margolis, E. D. Hinkley, and R. A. Toth, Appl. Opt. **16**, 523 (1977).
[7] N. Basco and R. D. Morse, J. Mol. Spectrosc. **15**, 35 (1973).
[8] Y. Matsumi, S. M. Shamsuddin, and M. Kawasaki, J. Chem. Phys. **101**, 8262 (1994).
[9] J. B. Nee and K. J. Hsu. J. Photochem. Photobiol. A: Chem. **55**, 269 (1991).
[10] M. T. Duignan and J. W. Hudgens, J. Chem. Phys. **82**, 4426 (1985).
[11] E. Bishenden and D. J. Donaldson, J. Chem. Phys. **101**, 9565 (1994).
[12] T. Baumert, J. L. Herek, and A. H. Zewail, J. Chem. Phys. **99**, 4430 (1993).
[13] J. A. Coxon, Can. J. Phys. **57**, 1538 (1979).
[14] J. B. Burkholder, P. D. Hammer, and C. J. Howard, J. Mol. Spectrosc. **124**, 139 (1987).
[15] S. Baumgärtel and K.-H. Gericke, Chem. Phys. Lett. **227**, 461 (1994).
[16] H. F. Davis and Y. T. Lee, J. Chem. Phys. **105**, 8124 (1996).
[17] R. F. Delmdahl, S. Baumgärtel, and K.-H. Gericke, J. Chem. Phys. **104**, 2883 (1996).
[18] A. Furlan, H. A. Scheld, and J. R. Huber, J. Chem. Phys. **106**, 6538 (1997).
[19] V. Vaida, E. C. Richard, A. Jefferson, L. A. Cooper, R. Flesch, and E. Rühl, Ber. Bunsenges. Phys. Chem. **96**, 391 (1992).
[20] E. Bishenden and D. J. Donaldson, J. Chem. Phys. **101**, 9565 (1994).
[21] B. E. Forch and C. N. Merrow, J. Chem. Phys. **95**, 3252 (1991).
[22] T. Kinugawa, T. Sato, T. Arikawa, Y. Matsumi, and M. Kawasaki, J. Chem. Phys. **93**, 3289 (1990).
[23] E. Rühl, A. Jefferson, and V. Vaida, J. Phys. Chem. **94**, 2990 (1990).
[24] K. Y. Choo and M. T. Leu, J. Phys. Chem. **89**, 4832 (1985).
[25] R. L. Miller, A. G. Suits, P. L. Houston, R. Toumi, J. A. Mack, and A. M. Wodtke, Science **263**, 1831 (1994).
[26] R. Toumi, P. L. Houston, and A. M. Wodtke, J. Chem. Phys. **104**, 775 (1996).
[27] R. I. Derby and W. S. Hutchinson, Inorg. Synth. **4**, 152 (1953).
[28] T. Haas, C. Maul, and K.-H. Gericke, Chem. Phys. Lett. **202**, 108 (1993).
[29] C. Maul, T. Haas, K.-H. Gericke, and F. J. Comes, J. Chem. Phys. **102**, 3238 (1995).
[30] I. P. Fischer, Trans. Faraday Soc. **63**, 684 (1967).
[31] M. Mons and I. Dimicoli, Chem. Phys. Lett. **131**, 298 (1986).
[32] J. R. Dubs, U. Brühlmann, and J. R. Huber, J. Chem. Phys. **84**, 3106 (1986).
[33] K. A. Peterson and H. J. Werner, J. Chem. Phys. **101**, 9565 (1992).
[34] K.-H. Gericke. Ph.D. thesis, Johann Wolfgang Goethe-Universität Frankfur Main, 1981.
[35] A. Wahner, G. S. Tyndall, and A. R. Ravishankara, J. Phys. Chem. **96**, 8948 (1992).
[36] R. Vasudev, R. N. Zare, and R. N. Dixon, J. Chem. Phys. **80**, 4863 (1984).
[37] R. Schinke, Comments At. Mol. Phys. **23**, 15 (1989).
[38] S. Solomon, Nature (London) **347**, 347 (1990).
[39] P. J. Crutzen and F. Arnold, Nature (London) **324**, 651 (1986).
[40] W. B. DeMore, S. P. Sander, D. M Golden, R. F. Hampson, M. J. Kurylo, C. J. Howard, A. R. Ravishankara, C. E. Kolb, and M. J. Molina. NASA Panel for Data Evaluation.